

Laser time-of-flight mass spectrometry for space

W. B. Brinckerhoff^{a)}

Applied Physics Laboratory, The Johns Hopkins University, Laurel, Maryland 20723-6099

G. G. Managadze

Space Research Institute (IKI), Moscow, Russia

R. W. McEntire, A. F. Cheng, and W. J. Green

Applied Physics Laboratory, The Johns Hopkins University, Laurel, Maryland 20723-6099

(Received 5 April 1999; accepted for publication 20 October 1999)

We describe a miniature reflection time-of-flight mass spectrometer for *in situ* planetary surface analysis. The laser ablation mass spectrometer (LAMS) measures the elemental and isotopic composition of regolith materials without any sample preparation or high-voltage source extraction. The small size ($<2 \times 10^3 \text{ cm}^3$) and low mass ($\sim 2 \text{ kg}$) of LAMS, due to its fully coaxial design and two-stage reflectron, satisfy the very strict resource limitations of landed science missions to solar system bodies. Microscopic surface samples are obtained with a short-pulse laser focused to a spot with a diameter $\sim 30\text{--}50 \mu\text{m}$. Coupled with a microimager, LAMS can interactively select and analyze a range of compositional regions (with lateral motion) and access unweathered, subsurface materials (with repeated pulses). The mass resolution is sufficient to distinguish isotopic peaks at unit masses, and the detection limits are on the order of a few ppm. The design and calibration method of a prototype LAMS device is given, including the development of preliminary relative sensitivity coefficients for major element bulk abundance measurements. © 2000 American Institute of Physics. [S0034-6748(00)00602-X]

I. INTRODUCTION

As the exploration of the solar system expands in depth and scope, the demand for miniature, yet fully capable, analytical instrumentation for space will increase. Mass spectrometers in particular, which can provide a complete chemical composition of all phases of matter, will continue to play a central role in orbiting,¹ descent,² and landed³ planetary missions. Several types of mass spectrometers for space, including sector, quadrupole, and time-of-flight (TOF) instruments, have been successfully flown or are under development. One of the major challenges for mass spectrometry in the next generation of landed missions to planets and small bodies will be the necessity to robotically analyze materials from a range of geological contexts. This *in situ* requirement will call for instruments with simple, robust design, little or no sample preparation, highly sensitive detectors, and a wide mass range. This last factor will be especially important for bodies such as Mars, Europa, and certain small bodies, where the detection of organic molecules may be a key scientific goal.

TOF-mass spectrometry (TOF-MS) is a particularly promising technique for *in situ* science. Gas-phase ions are detected with minimal attenuation compared to mass filters. Mass resolution and sensitivity are, in principle, independent of mass. The mass range is bounded only by the limits of detectability and recording time. Additionally, TOF-MS is ideal for analysis of solids due to its low sample usage, rapid, multichannel detection, and natural coupling with pulsed desorption. These features reduce the problem of elemental

fractionation observed in mass-scanning techniques. However, before the 1980s, the power of TOF-MS was limited by a broad temporal spread of ion formation (i.e., lack of a good “zero” time) and slow electronics. With the advent of short-pulse lasers and high-speed transient digitizers over the past two decades, these major limitations have been mostly overcome and TOF-MS is experiencing a renaissance in the analytical community.^{4,5} The development of miniature TOF-MS for space applications has thus entered a period of optimistic growth.

TOF-MS instruments detecting energetic ions and neutral atoms have flown on several missions, but have yet to be successfully deployed for surface analysis. The Russian PHOBOS mission carrying LIMA-D, a TOF-MS designed to study the surface of Phobos from a hovering distance of 30–80 m, unfortunately failed to reach its objective.⁶ Current efforts, such as use of the laser ablation mass spectrometer (LAMS) described in this article, primarily focus on lander or rover deployment scenarios. In the LAMS technique, the spectrometer is positioned over a microscopic field of view, chosen interactively with an optical imager, and a small volume of surface material is then evaporated and ionized with a pulsed laser. On atmosphereless bodies such as asteroids, no sample contact is required and forward contamination is eliminated. On bodies with an atmosphere, a minimal interaction is required to bring material into a vacuum chamber, but no further contact would be required by LAMS.

Following a description of the LAMS instrument and its operation in Sec. II, we present results for some different target materials, and discuss the process of abundance calibration for *in situ* quantitative analysis.

^{a)}Electronic mail: william.brinckerhoff@jhuapl.edu

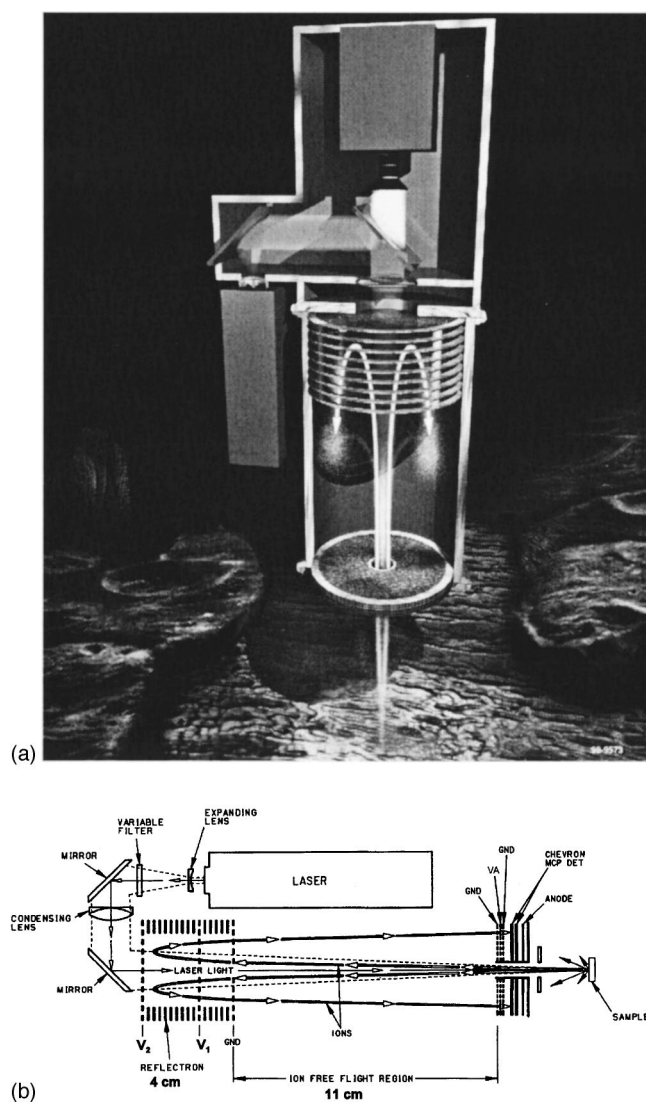


FIG. 1. (a) LAMS shown in orientation for *in situ* sampling, with a cutaway showing the internal design. (b) Instrument schematic. An ~ 8 ns pulse from the Nd:YAG laser is expanded, collimated, and directed through a focusing objective into the flight tube. The laser passes through the grids of the two-stage reflection, the free-flight region, and the hole in the center of the analytical grid/detector assembly to a focused spot of interest on the surface. Positive ions travel up through the same hole, are repelled by the reflectron, and strike the active surface of a microchannel plate at a sequence of times proportional to the square root of their mass-to-charge ratios.

II. EXPERIMENT

A. Laser ablation and ionization

The sampling method of LAMS is straightforward (Fig. 1). A Q -switched Nd:YAG laser, with infrared wavelength $\lambda = 1064$ nm and pulse duration $\tau = 8$ ns, is focused to a 30 – 50 μm diameter spot on the target surface *in vacuo*. In the laboratory system, small chip or pressed powder pellet targets (~ 2 mm across) are mounted on the end of a coaxial linear/rotary motion feedthrough (MDC K075-BRLM). The nominal operating pressure is 2×10^{-7} Torr. The position of the spot is chosen visually with a high-resolution camera that shares the laser's objective lens. A variable attenuator⁷ is used to control the irradiance I , normally between 0.5 and 5 GW cm^{-2} . In this range, the primary sampling process is

ablation, wherein material is evaporated and ejected from the target surface at a high rate, forming an expanding plume. During ablation, molecular structures are dissociated into their atomic constituents, and these vaporized atoms are subsequently ionized as they leave the surface during the laser pulse.⁸ Ionization occurs with varying efficiency and degree at ablation irradiances. It is desired to operate with a maximal, uniform ionization fraction (occurring at higher I) across all elements to best represent the abundances in the analyte.^{9–12} However, for the same reason it is also desirable to minimize production of multiply ionized atoms (also increasing with I), which can cause isobaric interferences in the time-of-flight detection. For instance, doubly ionized iron $^{56}\text{Fe}^{2+}$ will interfere with singly ionized silicon $^{28}\text{Si}^+$. This trade-off is not unduly restrictive. Empirically it has been found that laser irradiances of 1 – 2 GW cm^{-2} generate mostly singly charged ions with reproducible efficiency and sensitivity throughout the periodic table.⁹

Ablated ions leave the target surface with a distribution of kinetic energies ranging up to hundreds of eV. This distribution naturally depends on the laser power density and material composition, but is expected to remain constant for a given ionic species in a given specimen under fixed conditions. (The meaning of “fixed conditions” is discussed below.) In contrast with most laser time-of-flight instruments, LAMS does not “extract” ions from the target region by pre-accelerating them through a high potential difference. The purpose of extraction in other instruments is to increase the number of ions reaching the detector (via collimation) and to increase resolution by decreasing the relative spread of ion kinetic energies with respect to their mean energy. For example, in matrix assisted laser desorption/ionization (MALDI), the target backplate is set at a several kV positive potential with respect to a nearby grounded grid to extract low-abundance, high-mass species.¹³

In LAMS, the plasma plume generated at ablation irradiances tends to shield external fields from the ion source region, which would reduce the intended benefits of any pre-acceleration.^{14–16} Furthermore, pre-accelerated ions have shorter flight times that can strain the temporal resolution requirements in a miniature instrument. It is also generally desired to avoid high voltages and related design complexities and restrictions to permit laser ablation of unprepared surface materials in a direct, flexible fashion. LAMS is therefore designed to accept the natural kinetic energy distribution arising from the plume, and approaches the mass resolution issue solely through the use of ion energy focusing and windowing (see below). Low-energy analysis of the kinetic energy distribution of ablated ions under various conditions has proven to be useful for the understanding of matrix effects, selective fractionation, and ion interactions. Such information is vital for determining the optimal operating procedure for unknown specimens on remote missions, where high efficiency is required.

Ions with trajectories within approximately 3° from vertical pass through a hole in the center of the detector assembly and enter the LAMS flight tube (Fig. 1). These ions continue up in a field-free region until entering a coaxial reflectron (described next), where they experience a repel-

ling field due to grids at fixed electrostatic potentials. A fraction of the ions are turned around and impinge upon the active detector surface. The compactness of LAMS is partly due to this “fully coaxial” design. That is, the optical path of the laser and camera goes along the flight axis, *through* the reflectron grids, and through the centered hole in the detector assembly, normal to the target surface. The interaction between the defocused laser and the grids of the reflectron is negligible.

B. Energy focusing and windowing

The configuration of LAMS is similar to that of the LIMA-D and LASMA instruments.¹⁴ Ions travel from the target surface through a time-of-flight region and are detected by a dual microchannel plate (MCP) assembly at a sequence of times proportional to the square root of their mass-to-charge ratios. That is, $\text{TOF} \propto (m/z)^{1/2}$ for a given ion with mass m and positive charge z . The constant of proportionality depends of course on the initial energy of the ion and the particular path it takes through the spectrometer. It is generally desired to arrange for this constant to be the same for a given m/z over a wide range of energies, so that ions with the same mass arrive at the detector simultaneously. LAMS achieves such energy focusing with a second-order electrostatic ion mirror, or reflectron. As shown in Fig. 1, the reflectron consists of a stack of rings that define the above-mentioned repelling field. Mesh grids across three of these rings serve to divide the reflectron into two constant-field regions. The lowest grid is at ground, while the upper two are set at adjustable potentials V_1 and V_2 .

Now, whereas in the field-free, or free-flight, region the TOF varies with energy as $E^{-1/2}$, in the reflectron region the TOF varies as $E^{+1/2}$. By tuning the field profile in the reflectron via the grid voltages V_1 and V_2 , the time-of-flight dispersion at the position of the detector can be nearly eliminated over a wide energy range. Specifically, ions with higher E penetrate more deeply into the repelling field of the reflectron, and the extra time they spend in the reflectron permits lagging, lower-energy ions to “catch up” by the time the entire packet reaches the detector. The presence of the first stage grid V_1 simultaneously permits a wider range of energy focusing and allows the reflectron to be significantly shorter than the free-flight region. This means a miniature instrument can accommodate laser focusing over a rough surface and maintain high performance. The minimum free-flight distance is actually set by the necessary separation between the reflectron and the detector. In the LAMS laboratory development system, the reflectron length is only 4 cm, while the free-flight distance is 14–22 cm. As part of the free-flight distance is external to the flight tube, a flight version of LAMS is estimated at <20 cm total length.

The mass resolution R is determined by the temporal width of the arriving packet of ions with a given mass, relative to the time interval before arrival of the next mass. Equivalently, it may be expressed as $R = m/\Delta m = t/(2\Delta t)$, where Δt is the temporal width (say, at half maximum) of the ion packet and t its mean time of flight. To achieve “unit” mass resolution, where peaks at neighboring mass

numbers do not interfere,¹⁷ R should be in excess of 250 (achieved by LAMS). For free flight only, this would translate into a restriction on initial kinetic energy width of $\Delta E/E < 1/500$ but, with its two-stage reflectron, LAMS improves this to $\Delta E/E \approx 1/4$.

In practice, LAMS samples an energy band from the full distribution that is narrower than this theoretical limit. This is accomplished with a discrimination, or “analytical” three-grid assembly placed in front of the detector. The top and bottom grids are grounded, and the voltage V_A on the center grid is set such that $V_1 \leq V_A \leq V_2$, defining an acceptance window between V_A and V_2 . As such, only ions that reach the second stage of the reflectron ($V > V_1$) are detected. This windowing is desired to prevent unfocused ions from reaching the detector. In the present geometry the optimal focus is found at approximately $V_1 \approx 0.6V_2$ (see below), below the range where the reflectron TOF versus energy curve varies significantly.

Spectra are recorded by digitizing the current output of the MCP as a function of time after the laser pulse. TOF spectra are automatically converted into mass spectra using a scale coefficient calculated from the instrument dimensions and grid voltages. Neglecting the initial temporal and spatial spread of ions, as well as interactions between them, the LAMS TOF-to-mass scale for a particle with mass m and initial kinetic energy zV is given by

$$\left(\frac{2z}{m}\right)^{1/2} t = \frac{L_1 + L_2}{V^{1/2}} + \frac{4d_1}{V_1} [V^{1/2} - (V - V_1)^{1/2}] + \frac{4d_2}{V_2 - V_1} (V - V_1)^{1/2} + \frac{2(a_1 + a_2)}{V_A} [V^{1/2} - (V - V_A)^{1/2}] + \frac{2a_3}{|V_D|} [(V - V_D)^{1/2} - V^{1/2}], \quad (1)$$

where L_1 and L_2 make up the total free-flight distance (surface to reflectron, reflectron to detector), d_1 and d_2 are the lengths of the two reflectron regions, a_1 and a_2 are the distances separating the analytical grids, a_3 is the distance from the lower ground grid to the upper MCP, and V_D is the (negative) potential across the MCP. The accuracy and reproducibility of this scale are sufficiently high that calibration corrections are not required.

Neglecting the last two terms, as $(a_1 + a_2)/V_A$ and $a_3/|V_D|$ are small, and writing $c = V_1/V_2$ and $p = V/V_2$, the TOF expression may be approximated by

$$V_2^{1/2} \tau/L \approx \frac{1}{p^{1/2}} + \frac{4\delta_1}{c} [p^{1/2} - (p - c)^{1/2}] + \frac{4\delta_2}{1 - c} (p - c)^{1/2}, \quad (2)$$

where $\tau = (2z/m)^{1/2} t$, $L = L_1 + L_2$, $\delta_1 = d_1/L$, and $\delta_2 = d_2/L$. Figure 2, which plots Eq. (2) as a function of c for various $p > c$, demonstrates the presence of a high-order focus at $V_1 \approx 0.6V_2$. This point has been experimentally confirmed to high accuracy by LAMS. A small, reproducible correction for the time spent in the analytical grid region may be added to obtain elemental peak assignments that are

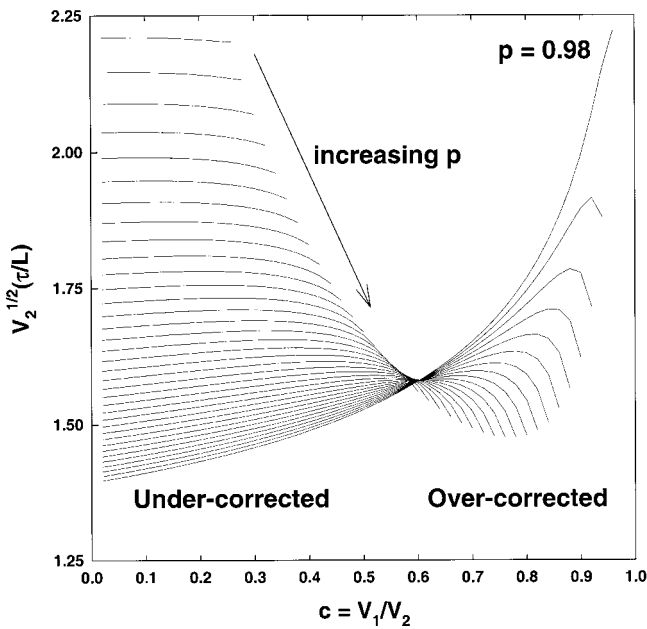


FIG. 2. Approximate one-dimensional model of the scaled TOF in LAMS as a function of $c = V_1/V_2$ for various $p = V/V_2$. Since ions with $V < V_A$ are rejected by the discrimination grids (see the text), only those with $V > V_A > V_1$, penetrating into the second reflection region, are shown.

reliable enough for autonomous operation. An example one-dimensional plot of ion trajectories (height y vs τ) is shown in Fig. 3. The ion energies in the plot range linearly from V_A to V_2 in 5 eV steps for clarity. A realistic distribution of trajectories would show a density of lines varying according to the window (V_A, V_2) on the intrinsic ion kinetic energies (often modeled as a modified Boltzmann distribution for ablation).

C. Detection and sensitivity

The microchannel plates are operated within the “current mode” range $1.6 \text{ kV} \leq |V_D| \leq 2 \text{ kV}$. The output current

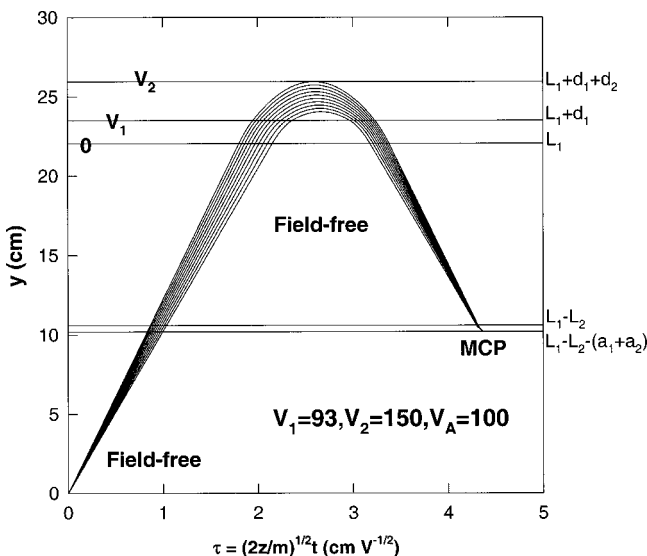


FIG. 3. One-dimensional model of the ion position as a function of scaled TOF for LAMS. Each trajectory represents an ion with a particular initial kinetic energy between V_A and V_2 . The energy step size shown in 5 eV for clarity.

as a function of time is digitized as a voltage by two channels of a Tektronix TDS 744A oscilloscope set at different gains. Signals exceeding the 8 bit range of the high-gain channel are stored as a low-gain value to give a net signal capability with a wide dynamic range. An entire spectrum is recorded in under $60 \mu\text{s}$. Shot to shot intervals are limited by data processing and the laser duty cycle. (Currently, LAMS records spectra at 0.1–0.2 Hz.)

The average transmission and sensitivity of LAMS may be estimated by working forward from the sample volume and backward from the measured MCP signal.¹⁸ For a rocky sample material of 2 g cm^{-3} , approximately 10^{13} atoms (1 ng) are ablated from the target surface. However, an average moderate-irradiance, narrow-window current versus time LAMS spectrum on a terrestrial basalt sample integrates to $\sim 5 \times 10^{-9} \text{ C}$, or $\sim 3 \times 10^{10}$ electrons. At the gain and efficiency of the MCP, this corresponds to $\sim 10^5$ ions detected over the TOF. The eight-order difference between ablation and detection is accounted for by the ionization efficiency and the transmission. The transmission attenuation is due to three factors: (1) the acceptance angle of the MCP hole, (2) the transparency of the grids, and (3) the energy window. We estimate the MCP aperture introduces a factor of $\sim 10^{-3}$ based on the 0.05 rad opening half angle and the expected forward plume bias. Approximately one order (10^{-1}) is caused by collisions with and scattering from the grids. The energy window factor is between 10^{-2} and 10^{-1} for narrow-window spectra. Therefore, the transmission is 10^{-6} – 10^{-5} . The average ionization efficiency is then approximately 10^{-2} – 10^{-3} . (The ionization efficiencies for particular species may vary, but they are expected to approach unity as the irradiance is increased above $\sim 1 \text{ GW cm}^{-2}$.) In conventional units, the sensitivity is $\sim 5 \text{ C g}^{-1}$.

III. RESULTS AND DISCUSSION

Our assessment of the quantitative capability of LAMS has involved measurements of a range of standard and unknown target materials of scientific interest (metals, rocks, clays, etc.). From standard materials, we can determine the relative sensitivity of LAMS to specific elements within a range of energy windows, and variations between matrix types. Unknown targets, presented as blinds, provide the best tests of the ability of LAMS to distinguish major subtypes (as in petrology or meteoritics) and of the limits of inferential mineralogy (probabilistic norms). All materials can be used to study isotope ratios. We present here results for the National Institute of Standards and Technology (NIST) standard reference material (SRM) C1154a steel (19Cr–13Ni stainless), a Co–W carbide, and a terrestrial desert basalt.

A. SRM C1154a steel

The known elements in SRM C1154a, as provided by NIST, are C, N, Si, P, S, V, Cr, Mn, Fe, Ni, Co, Cu, Nb, Mo, Ta, and Pb, and all but P, S, and Pb were detected within a few laser shots. In addition, the elements H, B, O, K, Ca, Sc, Zn, and As were regularly observed in well-defined energy ranges in both surface and at-depth spectra. We analyzed the relative elemental and isotopic sensitivities with a simple

TABLE I. Comparison of NIST and LAMS measured atomic abundances for SRM C1154a in various energy windows. Asterisks denote sums excluding the isobaric m/z peaks (50), (54), and (58): $V^*=(51)$, $Cr^*=(50)+(52)+(53)$, $Fe^*=(56)+(57)$, and $Ni^*=(60)+(61)+(62)+(64)$. NIST percentages with parentheses are not certified. Table entries with “...” did not have sufficient data to be calculated.

Element	NIST		(35, 45)		(45, 55)		(55, 65)		(65, 80)		(80, 110)		(110, 150)		(150, 200)	
	(wt. %)	(at. %)	\bar{x}	σ	\bar{x}	σ	\bar{x}	σ								
B	0	0	0.06	0.03	0.07	0.05	0.03	0.02	0.00	0.00
C	0.100	0.457	0.07	0.04	0.26	0.20	0.05	0.11
N	(0.077)	(0.302)	0.03	0.02	0.04	0.02
O	0	0	0.13	0.07	0.27	0.34	0.32	0.46	0.42	0.86	0.15	0.29
Si	0.530	1.035	0.94	...	0.63	...	0.34	0.10	0.00	0.06
P	0.060	0.106	0.015	0.009
S	0.051	0.087
Cl	0	0	0.02	0.02
K	0	0	0.14	0.11	0.03	0.04	0.08	0.08	0.01	0.08	0.35	0.20	0.90	0.65
Ca	0	0	0.05	0.03	0.69	0.33	2.14	0.97
Ti	(0.004)	(0.005)
V*	0.135	0.145	0.27	0.15	0.85	0.27	0.45	0.13	0.21	0.07	0.13	0.11	0.17	0.13	0.37	0.37
Cr	19.310	20.373
Cr*		19.888	12.81	4.52	17.82	3.43	16.92	2.89	15.49	3.23	19.22	3.64	13.62	2.76	13.08	5.37
(54)		4.146	4.59	0.31	4.23	0.72	4.10	0.40	4.02	0.34	4.05	0.43	4.26	0.42	4.86	0.69
Mn	1.440	1.438	2.27	1.01	4.68	1.34	2.66	0.98	1.56	0.49	1.70	0.56	1.73	0.82	2.21	1.44
Fe	64.043	62.908
Fe*		59.039	63.22	3.87	58.01	1.77	63.97	4.16	62.83	5.09	62.69	4.15	60.15	3.39	60.90	10.24
(58)		8.502	9.63	1.51	7.64	1.58	7.74	1.46	8.25	1.27	7.99	0.88	8.86	1.17	8.99	1.80
Ni	13.080	12.224
Ni*		3.934	4.60	0.86	3.94	0.88	3.67	0.67	4.02	0.75	3.73	0.78	5.33	0.89	6.57	1.56
Co	0.380	0.354	0.65	0.16	1.09	0.40	0.87	0.35	0.58	0.15	0.43	0.11	0.60	0.11	0.78	0.24
Cu	0.440	0.380	0.43	0.08	0.44	0.12	0.38	0.14	0.45	0.15	0.29	0.23	0.74	0.21	1.01	0.56
As	0	0	0.11	0.03	0.05	0.04	0.00	0.13	0.05	0.05	0.08	0.11	0.55	0.20	1.09	0.69
Nb	(0.220)	(0.130)	0.10	0.26	0.43	0.31	0.52	0.94	2.08	3.41	0.45	0.25	1.65	0.74	2.93	2.39
Mo	0.068	0.039
Ta	(0.045)	(0.014)
Pb	0.017	0.005
Mean TDY			59.90		37.04		27.46		29.02		33.82		40.47		42.34	

protocol as follows. First, the reflectron voltages were set to a particular energy band-pass window, beginning with highest range of $(V_A, V_2)=(150,200)$ V. The sample height was adjusted so that the surface was slightly below the laser focus (minimum beam waist diameter). With the detector voltage at a fixed $V_D=1.8$ kV, the laser power was varied until clear, reproducible spectra were observed. This “working” laser power was set between the points where the singly and doubly ionized peaks were just visible above the background. In SRM C1154a, the dominant $^{56}Fe^+$ peak was always the first signal to appear at low power and among the first peaks to appear doubly ionized at higher power. (Recognizing spectra where $^{56}Fe^{2+}$ interfered with $^{28}Si^+$ was not a problem, as the isotopes of Fe and Cr were observed to doubly ionize as a group, producing a different peak pattern than that of the Si isotopes.) A series of 50 TOF spectra were then recorded, mass scaled, and integrated, and the procedure repeated for each of the seven windows: $(V_A, V_2)=(150,200)$, (110, 150), (80, 110), (65, 80), (55, 65), (45, 55), and (35, 45) V. Spectra below 35 V required a significant decrease in laser energy and contained many broadened and asymmetrical peak shapes. These could not be analyzed in equal terms with the other windows and were neglected in this initial study.

Table I compares the measured LAMS signal in the seven energy windows to the values provided by NIST for

this target. In the first column, elements denoted by asterisks (V, Cr, Fe, and Ni) exclude the isobaric isotope peaks m/z (54) and (58). The values for these shared peaks are compared to $(54)=^{54}Cr+^{54}Fe$ and $(58)=^{58}Fe+^{58}Ni$ using standard terrestrial isotopic abundances. In the case of m/z (50), the small fraction (3.5×10^{-6}) due to V was neglected. The NIST weight and atomic percentages are given in the second and third columns, with uncertified values in parentheses. As the LAMS signal is a current proportional to the number of detected ions, measured values should be compared to the atomic percentage. The Table I entries are averages of raw signal integrals as ratios of the total detected ion yield (TDY). The TDY is the raw signal integral over the entire TOF range, above a fitted baseline. It may be considered an empirical proxy to the output of the complex ablation and ionization processes in LAMS. Entries denoted as “...” denote insufficient data and/or failed peak detection.

The results in Table I are from the subset of the 50 laser shots within the range $10 < TDY < 100$. Below $TDY \sim 10$, only the major peaks of Cr, Fe, and Ni were observed, and quantitative results were extremely sensitive to baseline fitting. Above $TDY \sim 100$, the major peaks tended to saturate the low-gain channel of the oscilloscope, precluding a major-to-minor element comparison and any absolute percentages. The number of spectra averaged thus ranged from 31 to 45.

As may be inferred from Table I, relative elemental sen-

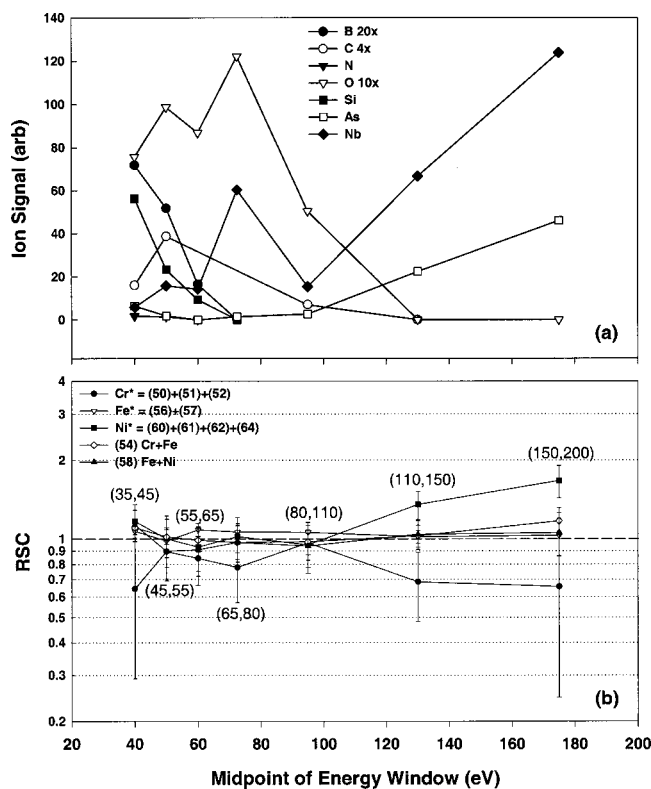


FIG. 4. LAMS results for NIST SRM C1154a steel. (a) Net ion signal vs kinetic energy window midpoint for B, C, N, O, Si, As, and Nb. The B, C, and O points are scaled for clarity. (b) RSC calculated as the ratio of measured to expected atomic abundance for Cr, Fe, and Ni. Major isobaric m/z values 54 and 58 are evaluated separately using standard terrestrial isotopic percentages. The points are positioned at energy midpoints, and the window endpoints are shown as (V_A, V_2) .

sivities and abundance precision depended strongly on the ion kinetic energy range. The lowest-mass elements (B through P) were only found in the lower-energy windows. Individual-window abundances for C, N, Si, and P fell significantly below their known bulk values. This observation is in agreement with results from another NIST steel sample,¹⁹ and with the expectation that lower-mass ions generally have lower mean kinetic energies in laser ablation.²⁰ The total LAMS signals (abundance weighted by mean TDY) for seven elements are plotted as a function of energy window midpoint in Fig. 4(a). B, C, and O data are scaled for clarity.

Interpreted as kinetic energy spectra, the signals for C and O correspond to distributions with means of ≤ 50 –70 and ~ 50 –80 eV, respectively. These means are upper bounds, as they assume that the behavior below (35, 45) eV is a simple extension of the observed trends. In fact, there is preliminary evidence²¹ for a large increase in carbon ions below 30 eV in NIST steels. The total carbon integral is thus expected to be closer to the expected value than the limited energy range data presented here. Similarly, the signals for B and Si increase for lower energies, implying spectra with means below (35, 45) eV.

Heavier elements (K through Nb) were detected across the entire energy range measured. The highest-mass elements observed reproducibly (As and Nb) were increasingly prevalent with increasing energy, as expected [Fig. 4(a)]. In the (35, 45) eV band, ⁹³Nb was emitted with an approximately accurate atomic abundance, but it increased to more than 20 times the expected value at the highest energies, in agreement with the behavior of the neighboring element Mo in another NIST steel.^{19,22} This increase may be due to more than individual window fractionation alone. Within the energy range scanned, the “total” relative resistivity coefficients (RSCs) (from the signal summed over all the windows) for the heavy elements were also anomalously high.

The major transition metal elements V through Cu were directly accurate to within 5%–20% in several energy windows. The ratios of measured to expected atomic percentage, or RSCs, for the major elements Cr, Fe, and Ni are plotted as a function of the energy window midpoint in Fig. 4(b). The error bars correspond to one standard deviation. The observed RSC values for these elements suggest flatter energy spectra than those seen for the minor elements. Of particular note is the enhanced accuracy and precision for these elements in the band (80, 110) eV. The best average accuracy for the minor transition metals V, Mn, Co, and Cu (not plotted) also coincided with this window, where all four elements exhibited broad minima in their TDY-weighted signals. This energy spectrum minimum, which follows from the mean TDY variation (Table I), may be an intrinsic feature of laser-ablated metals, exhibiting “thermal” (~ 10 eV) and “accelerated” (~ 100 eV) energy peaks.^{9,23}

In Table II, the measured minor isotopic abundances are compared to standard terrestrial values. Ratios were taken

TABLE II. Comparison of standard and measured minor isotopic abundances in SRM C1154a for various energy windows.

Elements	Std %	(35, 45)		(45, 55)		(55, 65)		(65, 80)		(80, 110)		(110, 150)		(150, 200)	
		\bar{x}	σ	\bar{x}	σ	\bar{x}	σ								
¹⁰ B	18.98	20.19	4.91	21.38	6.43
¹³ C	1.11	1.28	0.76	1.14	0.06	1.20	0.18	1.28
²⁹ Si	4.71	5.53	0.04	5.73	0.30	5.55	0.18
³⁰ Si	3.12	2.97	0.42	3.86	1.12	2.72	0.17
³⁷ Cl	24.23	24.48	1.85	24.99	0.40
⁵⁰ Cr*	4.40	4.11	0.38	3.73	0.34	3.72	0.38	3.78	0.39	3.28	0.40	4.39	1.18	6.73	1.97
⁵³ Cr*	9.78	10.01	2.10	13.67	3.79	11.00	2.79	9.75	2.83	8.69	1.48	9.90	2.30	12.90	2.67
⁵⁷ Fe*	2.33	4.02	0.89	7.74	1.68	3.92	0.99	3.06	0.86	2.67	1.01	3.03	0.58	4.05	1.16
⁶¹ Ni*	3.70	6.37	1.28	8.67	1.79	8.72	2.32	5.15	1.04	4.45	1.72	5.54	1.82	6.30	2.05
⁶² Ni*	11.38	12.31	1.71	11.58	1.86	12.66	2.20	12.73	2.06	11.50	0.90	13.24	1.94	15.63	2.60
⁶⁴ Ni*	3.36	4.31	0.59	4.09	1.04	4.08	1.17	3.90	1.21	2.84	0.65	4.82	2.04	5.46	2.78
⁶⁵ Cu	30.91	32.23	6.97	30.32	6.22	31.26	9.41	30.95	6.90	29.34	4.88	31.07	3.08	29.72	2.36

with respect to the total elemental detected yield (EDY), or for elements with isobaric interferences, the unambiguous subtotal (as introduced above). Performance without any standardization or elemental envelope adjustment was very good. Ratios for ^{10}B , ^{13}C , ^{37}Cl , ^{50}Cr , ^{62}Ni , and ^{65}Cu had an uncorrected average accuracy of less than 7%. Energy-dependent isotopic fractionation is not expected to be as significant as it is for elements, but some marked anomalies did occur in the (45, 55) and (150, 200) eV range. It was discovered that, in these cases, the number of spectra in which isotope measurements could be reliably made was reduced. Increasing counting statistics for averaging will probably smooth the observed sensitivity trends. Isotopic abundance accuracy for these elements increased with separation from the dominant ^{56}Fe peak, implying that baseline and peak shape sensitivity introduced systematic errors. A striking example of this effect is the $^{65}\text{Cu}/\text{Cu}$ value, with an average standard deviation of 2.4%. The total Cu content of C1154a is only 0.38 at. %, but the absence of any broadened neighboring peaks permitted a highly reproducible measurement. Isotopic accuracy for the minor elements also increased with EDY, as expected, given the constancy of the baseline noise. For those spectra in the top 10% of the EDY range for a given minor element, sub-1% errors were regularly observed (although insufficient data were obtained in this range to calculate σ).

The single-shot detection limit in SRM C1154a was estimated as 18 ppm atom by the detection of ^{34}S with a signal-to-noise ratio of 2. Due to the high reproducibility of the peak positions, automated averaging of spectra should provide improvements approaching the $N^{-1/2}$ dependence with random noise. The average resolution for most peaks in the low-mass range was $m/\Delta m \sim 200$ using the half-width at half-maximum definition.

The overall performance with this standard steel was quite encouraging, given the modest number of spectra averaged and the ability of the small laser spot to sample the heterogeneity of the target. The elemental and isotopic accuracy equals or exceeds that of other laser mass spectrometric methods when no standards are used.¹¹ The middle energy range of high reproducibility indicates that a LAMS calibration can be obtained for accurate measurement of “neighboring” elements within a single energy window, reducing the overall energy scanning. The narrow-window view works well here for absolute abundances because this neighboring element sequence comprises the vast majority of atoms in the solid. More generally, such a calibration would be most suitable for nearby-element ratios (e.g., to Fe), which are not sensitive to absolute fluctuations of the considered mass range.

To better understand the fractionation behavior of low-energy ions in LAMS, we performed a separate analysis of a Co–W carbide target. Due to the simpler stoichiometry of the carbide relative to C1154a, we were able to obtain reproducible elemental yields to below 10 eV, with 5 eV windows. A sensitivity much closer to the total RSC could thus be obtained by integrating the entire energy range. A simple scan was recorded from a fresh surface for each of two incident laser irradiances, $I_1 = 0.77 \text{ GW cm}^{-2}$ and I_2

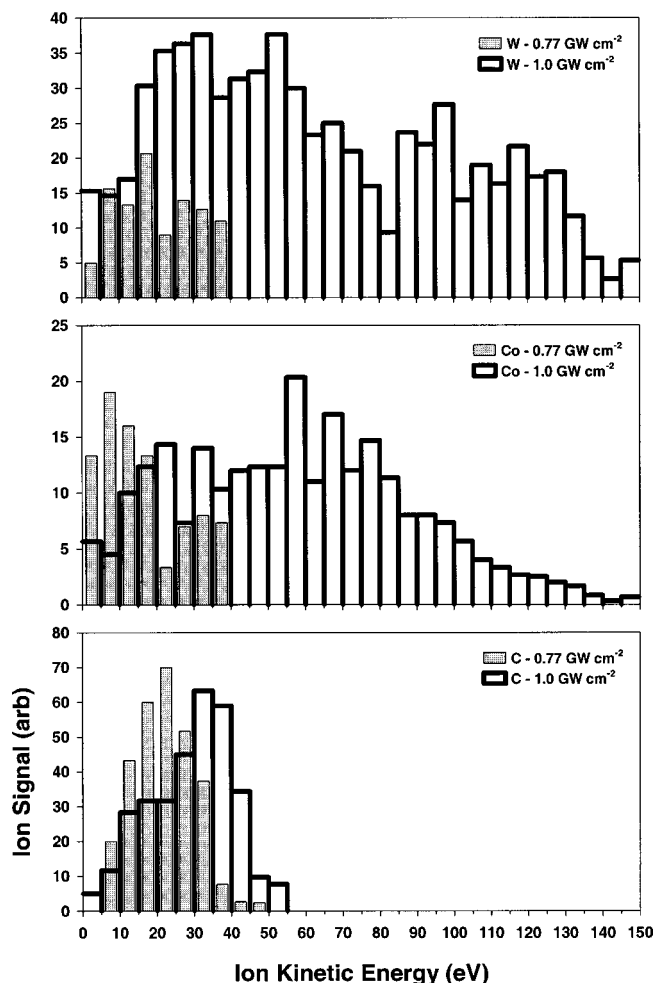


FIG. 5. Ion kinetic energy spectra for C, Co, and W in a carbide LAMS target. The energy range was scanned in 5 eV steps for each of the two laser irradiances ($I_1 = 0.77 \text{ GW cm}^{-2}$ and $I_2 = 1.0 \text{ GW cm}^{-2}$).

$= 1.0 \text{ GW cm}^{-2}$. Figure 5 shows the raw distributions obtained for the three elements C, Co, and W. These elements are well separated in the TOF spectra (mean $m/z = 12$, 59, and 184 amu/e), and their low-energy spectra were unambiguously integrated. The plots demonstrate the sensitivity of ionization to the species and the laser power density. As expected from the NIST steel studies, C was found almost entirely below 50 eV. The total carbon signal increased by only a factor of 1.11 from I_1 to I_2 (from 295 to 327), while the Co and W signals increased manyfold (2.86 and 7.29 times, respectively). When compared to the certified atomic abundance ratios (C/Co 1.36, C/W 1.29), there was a large relative excess of C (C/Co 3.38, C/W 2.91) at low irradiance, but W/Co was accurate to within 10%. At high irradiance, there was a relative excess of W, but C/Co agreed to within 3% (C/Co 1.31, C/W 0.44).

The irradiances used here are near the lower end of the “hot plasma” range,⁹ in which the ionization efficiency is fairly uniform and near 100%, and the ablation mass is proportional to $I^{1/2}/m^{1/4}$. For a given laser shot in this range, higher-mass atoms are ablated less efficiently (although weakly so). However, Co and W also have lower ionization potentials than C. At irradiances below $\sim 1 \text{ GW cm}^{-2}$, the fractions of ablated Co and W atoms that are ionized will be

enhanced, countering the ablation mass trend. (Above ~ 1 GW cm $^{-2}$, the dependence on the ionization potential dissipates.)²⁴ Thus the irradiance regime used may host competing fractionation trends, with total RSCs that are quite sensitive to fluctuations in laser coupling and sample heterogeneity. The increases in Co/C and W/C with I may indicate that the “hot” range is attained for Co and W at lower irradiance than for C. This trend is consistent with the anomalously high total RSCs for higher-mass elements seen in other targets. The high-irradiance W ion energies also exhibited a double-peaked distribution, with means of ~ 40 – 50 and ~ 110 – 120 eV. The complexity introduced by the sensitivity to irradiance and by possible multimodal energy spectra²⁵ indicates that any autonomous operation of LAMS should include a general scan of a wide energy range, in addition to sequences of shots within select narrow windows as described above.

B. Terrestrial basalt

As a more realistic target for future *in situ* studies, we have begun to examine a terrestrial desert basalt sample with LAMS. The specimen was presented as a “partial” blind (the exact origin and mineralogy have not been disclosed), and the subclassification analysis is ongoing. Preliminary studies of the basalt have already been quite helpful in assessing the reproducibility of elemental and isotopic yields, as well as the ability of LAMS to probe into the subsurface layers of rocky materials.

Detected elements were H, C, O, Na, Mg, Al, Si, P, K, Ca, Ti, V, Mn, Fe, and a few rare earths at trace levels. Spectra were clearly distinguishable between surface and bulk types and between “high Fe” and “low Fe” within the bulk. Sequences recorded at a fixed location, but at varying depths, changed between high-Fe and low-Fe types within a few shots, similar to the behavior seen in a carbonaceous chondrite target.¹⁹ Figure 6(a) shows an example single-shot bulk spectrum from the basalt target in the energy window (65, 75) eV. It is typical of the high-Fe bulk regions (atomic Fe/Si > 3 , vs the ~ 0.2 expected) observed in approximately 1/3 of the spectra in this range. The low-Fe spectra comprising the remaining bulk measurements were clustered around Fe/Si ~ 1 . Averaged abundance ratios therefore reflect the strong fractionation bias (in this narrow energy range) toward higher masses as seen in other targets. Similarly, the spectra were markedly low in O (atomic O/Si < 0.5 versus the ~ 3 expected).

Isotopic ratios were more accurate and reproducible in this target than in any of the metal alloys examined. The minor isotope abundances in the Mg–Ti series agreed to within 5%, the maximum observed standard deviation of raw signal ratios. Figure 6(b) shows Ti isotope data for 22 laser shots. The increase in relative sensitivity from -5% to $+5\%$ may reflect an intrinsic bias toward higher masses, as was seen in SRM C1154a, but over a much narrower mass range. This trend was slightly modulated according to the baseline fitting method, but the overall errors were stable. Highly reproducible and accurate isotope ratios in this mass range were also observed in a carbonaceous chondrite meteorite.¹⁹

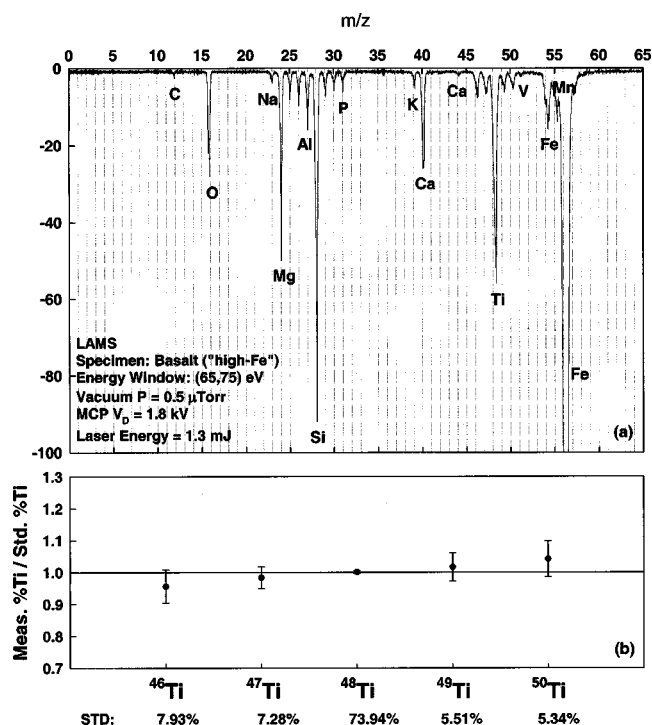


FIG. 6. Terrestrial desert basalt results from LAMS. (a) Sample single-shot spectrum from a “dark” bulk region in the energy window (65, 75) eV. (b) Measured isotopic abundances for Ti compared to expected terrestrial values in basalt. Standard percentages are shown below the isotope masses. The error bars correspond to one standard deviation for 22 laser shots.

The potential to distinguish mineralogical regions with LAMS has led to a focus on surface layer analyses. Surface layers on rocky materials are known to arise from various processes reflective of the interaction of the material with its environment over time. By microscopically studying a rock from its surface inward, we may infer the history of aqueous, wind-borne, biogenic, and other processes in the vicinity of the exposed surface. This analysis is of particular importance for *in situ* probes, which must access material within and below a weathered surface, to properly determine the rock type and geological context. The basalt target (observed through the LAMS imager) had a mottled surface indicative of weathering. We examined a sequence of 150 spectra in a (140, 150) eV window from a fresh surface to see if a rock varnish²⁶ could be detected from LAMS spectra. The raw atomic Mn/Fe, (Na+K)/Si, and Al/Si ratios were monitored in real time and plotted (Fig. 7).

Nearly every spectrum contained Mn and Fe, while approximately 20 out of the 150 shots did not generate sufficient signal to measure the Na+K and Al ratios, giving those plots a more decimated appearance. The Mn/Fe ratio began at a high, constant value (> 1), then dropped precipitously after ~ 70 shots to a value more in line with terrestrial basalts. With the estimated 0.2 – 0.3 μm per shot, the detected layer was ~ 15 – 20 μm thick. This is the expected behavior for varnish layers, which are known to be high in Mn due to the presence of a manganese oxide known as birnessite.²⁶ Due to the usual inclusion of Na and K atoms in this mineral, the atomic ratio of (Na+K)/Si was also of interest. From the plot, it clearly had similar behavior to Mn/Fe. Since the Si

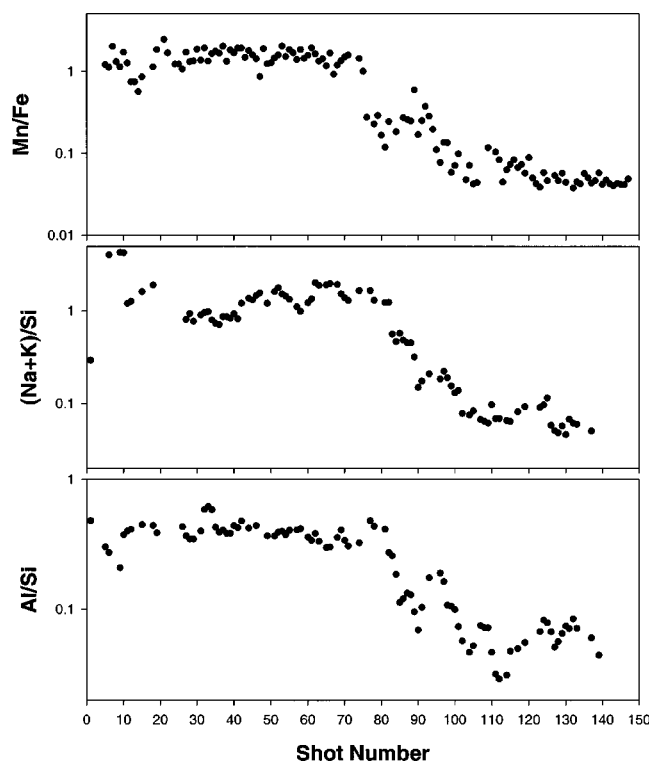


FIG. 7. Monitored total element atomic ratios in basalt as a function of laser shot number from an unanalyzed weathered surface. The vertical scale is logarithmic. The ablated (crater) depth is approximately $0.2\text{--}0.3\ \mu\text{m}$ per shot.

abundance was constant, within experimental precision, over the entire sequence, the transition is between regions of high and low Na+K. The “bulk” value of $(\text{Na}+\text{K})/\text{Si}\sim 0.07$ is lower than, but comparable to, the expected range for basalts ($\sim 0.11\text{--}0.13$).²⁷ The third ratio monitored, Al/Si, shows the same qualitative behavior, with a highly reproducible varnish layer value of ~ 0.4 , but with a less pronounced drop into the bulk phase than the other two ratios. We are not aware of a high aluminum oxide characteristic of rock varnish, and this is the only other element ratio that showed a significant layer transition. (Conspicuously absent was a variation in C. High C from magnetotactic bacteria discussed in some theories of rock varnish would be expected to drop in the bulk phase. However, almost no C was detected in the high energy window used here.)

C. Instrument outlook

The results for LAMS thus far are very encouraging for high sensitivity and quantitatively based *in situ* classification of major rock and soil types. The highly miniaturized design of LAMS also permits its use in a multicontext mission, where several samples are taken from a wide area. The depth ability with the basalt demonstrates LAMS access to bulk, unweathered material. The degree of accuracy and precision in science return from a mission including LAMS will depend both on the overall instrument suite (the complementarity of multiple detectors), and on *a priori* knowledge of the intrinsic relative sensitivities in LAMS. The initial calibration of RSCs on standard and unknown targets has been described in this article. A much wider range of experimental

conditions and materials is currently under investigation, and should lead to a “flight-ready” approach for unknown *in situ* samples.

Determining the empirical relationship between the LAMS detector output and the elemental and isotopic abundances within the analyte is the goal for assessing quantitative ability. The relative sensitivity coefficient is, in general, a function of the laser-target coupling, the target composition, and the LAMS ion optics and detection parameters. A good RSC calibration clearly depends on understanding the reproducibility of experimental conditions.²⁸ The ion optics and detection setup generate a fractionation that is expected to be small and reproducible for any material. Further, for bulk averages, the use of laser irradiances slightly above $\sim 1\ \text{GW cm}^{-2}$ gives high, uniform ablation and ionization efficiencies across many target types. However, the variation in laser-target coupling may lead to irreproducible experimental conditions in some cases. In particular, surface morphology fluctuations can change characteristics of the plume from shot to shot, and thus ablation is often viewed as unpredictable. For appropriately defined averages, though, reproducibility may be restored and an “intrinsic” instrumental RSC may be observed. For instance, abundances within small grains may be obtained by averaging enough spectra to detect all variations from the bulk, but few enough to remain within the grain. As such, the specific requirements for quantitative analysis with LAMS may depend on the composition information desired.

All analyses use a common energy windowing and focusing method based on the instrument description above. Normally, several windows (V_A , V_2) are used to sample the kinetic energy distribution of emitted ionized species. The peak energies and widths of these distributions generally increase with mass, laser irradiance, and degree of ionization. For a fairly constant irradiance and single-stage ionization, spectra can be recorded and single mass peaks integrated assuming a fixed energy distribution.

Important low-mass ions such as C^+ , N^+ , and O^+ are concentrated at kinetic energies below 50 eV. It is expected that special window modes, such as calibrated combinations of narrow- and wide-window spectra, will be required to achieve the precision and sensitivity needed to address *in situ* science goals. In the laboratory prototype of LAMS, these elements may be present in the residual vacuum chamber gas. The redeposition of these elements following a laser shot can increase their effective detection limit. We are currently investigating this process with a variable-delay double-pulse laser that first removes surface contaminants and then analyzes bulk material before significant redeposition can occur.²⁹ Such “pre-cleaning” may allow closer simulation of the conditions of *in situ* analyses.

In addition to understanding the behavior of the current LAMS instrument with a range of target materials, efforts are underway to improve the sensitivity and resolution of LAMS itself. Incorporating an Einzel lens (or other ion lens) will increase the throughput via collimation. In LAMS the position and voltage range of lenses must be carefully adjusted to avoid complications due to the plasma plume. Similarly, a pulsed ion gate will permit the selective suppression of cer-

tain TOF regions to minimize any ion interaction difficulties and increase sensitivity. It too must be reexamined for miniature instrument use. The size limitations in planetary exploration also restrict the flexibility in reflectron design. Tests are currently underway with ideal, or nearly ideal, reflectron designs that correct the TOF over a much wider energy range than the two-stage LAMS unit. High-order correction in LAMS demands that component positions and electrostatic parameters be highly precise and robust.

Finally, we are testing LAMS with an ultraviolet (UV) Nd:YAG tripled (355 nm) or quadrupled (266 nm) laser that may increase its sensitivity to various species, including molecular compounds. Shorter wavelengths may also produce a smaller and more reproducible crater. However, any improvement with UV must be weighed against the increased complexity and fragility that may be required in a flight unit. The infrared (IR) laser was originally chosen to test the simplest LAMS that can provide useful results on future missions. We plan to provide a quantitative comparison of UV ablation (as found in some commercial instruments) and UV desorption (such as in MALDI-type systems) in LAMS with the IR results in a future report.

ACKNOWLEDGMENTS

The authors wish to acknowledge the advice and assistance of Dr. R. E. Gold, Dr. E. H. Darlington, Dr. E. P. Keath, Dr. S. L. Murchie, Mr. D. A. Lohr, Dr. D. E. Brownlee, and Dr. D. S. Burnett. One of the authors (G.G.M.) wishes to thank A. E. Chumikov, N. G. Managadze, and V. Leonov, and Advanced Power Technologies, Inc. (APTI), which is developing a commercial version of the LASMA device. This work was supported by NASA Planetary Instrumentation Definition and Development Program (PIDDP) Grant No. NAG5-4548, and by APL Independent Research and Development funding.

- ¹H. B. Niemann, J. R. Booth, J. E. Cooley, R. E. Hartle, W. T. Kasprzak, N. W. Spencer, S. H. Way, D. M. Hunter, and G. R. Carignan, *IEEE Trans. Geosci. Remote Sens.* **GE-18**, 60 (1980); R. W. McEntire and D. G. Mitchell, in *Solar System Plasma Physics*, edited by J. H. Waite, J. L. Burch, and R. L. Moore, Geophysical Monograph Series (The American Geophysical Union, Washington, DC, 1989), Vol. 54; W. Kasprzak, H. Niemann, D. Harpold, J. Richards, H. Manning, E. Patrick, and P. Mahaffy, *Proc. SPIE* **2803**, 129 (1996); P. R. Mahaffy, in *Laboratory Astrophysics and Space Research*, edited by P. Ehrenfreund *et al.* (Kluwer, Dordrecht, 1998), p. 355; S. Scherer, K. Altwegg, H. Balsiger, M. Hohl, H. Kastle, M. Mildner, and P. Wurz, *Proceedings of the 46th ASMS Conference on Mass Spectrometry and Allied Topics*, Orlando, FL, 1998, p. 1238.
- ²H. B. Niemann, D. N. Harpold, S. K. Atreya, G. R. Carignan, D. M. Hunten, and T. C. Owen, *Space Sci. Rev.* **60**, 111 (1992); H. B. Niemann, in *Gas Chromatograph Mass Spectrometer for the Huygens Probe* [European Space Agency (ESA)-SP-1177, 1997], p. 85; V. Navale, D. Harpold, and A. Vertes, *Anal. Chem.* **70**, 689 (1998).
- ³R. D. Rushneck, *et al.*, *Rev. Sci. Instrum.* **49**, 817 (1978); Planetary Science Instruments Workshop, edited by C. Meyer, A. H. Treimann, and T. Kostiuk, LPI Technical Report No. 95-05, Lunar and Planetary Institute, Houston, 1996.
- ⁴R. J. Cotter, *Time of Flight Mass Spectrometry: Instrumentation and Applications in Biological Research* (American Chemical Society, Washington, DC, 1997).
- ⁵*Laser Ionization Mass Analysis*, edited by A. Vertes, R. Gijbels, and F. Adams (Wiley, New York, 1993).
- ⁶R. Z. Sagdeev, G. G. Managadze, I. Yu. Shutyaev, K. Szego, and P. P. Timofeev, *Adv. Space Res.* **5**, 111 (1985); R. Z. Sagdeev *et al.*, *Proceedings of the International Workshop on Phobos*, Space Research Institute (IKI), USSR Academy of Sciences, Moscow, 1986, p. 7.
- ⁷The attenuator (a Spindler and Hoyer neutral wedge) consisted of a neutral density glass wedge bonded to a clear compensating plate. The transmission could be varied between 1% and 80% with a precision translation stage, although we typically operated at the high-transmission end, where the attenuation drop across the beam diameter was negligible. To obtain highly attenuated pulses, we used additional flat neutral density filters in the beam path.
- ⁸In contrast to ablation, lower laser irradiances ($I < 10^8 \text{ W cm}^{-2}$) sample target material by an assortment of thermal and nonthermal processes termed laser desorption. In the desorption regime, molecules and molecular fragments survive volatilization and ionization, producing spectra containing both atomic and molecular information. Depending upon irradiance and target matrix effects, identification of large molecular species including organic/biological structures is possible with desorption. The natural extension of LAMS to this lower-energy range is currently under investigation.
- ⁹C. R. Phipps and R. W. Dreyfus, in Ref. 5, Chap. 4A.
- ¹⁰L. Moenke-Blankenburg, in Ref. 5, Chap. 4B.
- ¹¹H.-J. Dietze and J. S. Becker, in Ref. 5, Chap. 4C.
- ¹²L. Moenke-Blankenburg, in *Lasers in Analytical Atomic Spectroscopy*, edited by J. Sneddon, T. L. Thiem, and Y.-I. Lee (VCH, New York, 1997), Chap. 4.
- ¹³K. Tanaka, Y. Ido, S. Akita, Y. Yoshida, and T. Yoshida, *Rapid Commun. Mass Spectrom.* **2**, 151 (1988); M. Karas and F. Hillenkamp, *Anal. Chem.* **60**, 2299 (1988).
- ¹⁴G. G. Managadze and I. Yu. Shutyaev, in Ref. 5, Chap. 5.
- ¹⁵R. Z. Sagdeev *et al.*, *Astron. Astrophys.* **187**, 179 (1987).
- ¹⁶I. D. Kovalev, N. V. Larin, A. I. Suchkov, A. M. Voronov, and P. A. Shmonin, *Prib. Tekh. Eksp.* **6**, 139 (1985).
- ¹⁷Unit mass resolution is sufficient to resolve the isotopes of any given element from each other, but is not sufficient to resolve *isobars*, i.e., the isotopes of different elements sharing the same mass number. Isobaric interferences may also arise if molecular species coincide with atomic ions, e.g., ^{18}O and H_2O . To separate such contributions, resolutions of 10^3 – 10^4 are often required. For laser TOF-mass spectrometers, it may be more realistic to focus on elemental and isotopic enrichment techniques for *in situ* isobaric resolution. Examples of such techniques include chemical separation, negative-ion generation, and resonance ionization.
- ¹⁸O. J. Orient, A. Chutjian, and V. Garkanian, *Rev. Sci. Instrum.* **68**, 1393 (1997).
- ¹⁹W. B. Brinckerhoff, A. F. Cheng, R. W. McEntire, and G. G. Managadze, in *Lunar and Planetary Science XXIX*, Abstract No. 1789 (Lunar and Planetary Institute, Houston, 1998).
- ²⁰J. T. Cheung and H. Sankur, *Crit. Rev. Solid State Mater. Sci.* **15**, 63 (1988).
- ²¹Unpublished results.
- ²²W. B. Brinckerhoff, R. W. McEntire, A. F. Cheng, and G. G. Managadze, *Third IAA Conference on Low-Cost Planetary Missions* (International Academy of Astronautics, Pasadena, CA, 1998).
- ²³Yu. A. Bykovskii, G. I. Schuralev, V. I. Belousov, V. M. Gladskoi, V. G. Degtjarev, Yu. N. Kolosov, and V. N. Nevolin, *Fiz. Plazmy* **4**, 323 (1978).
- ²⁴A. Vertes, P. Juhasz, M. De Wolf, and R. Gijbels, *Int. J. Mass Spectrom. Ion Processes* **94**, 63 (1989).
- ²⁵Q. Zhuang, K. Ishigoh, K. Tanaka, K. Kawano, and R. Nakata, *Jpn. J. Appl. Phys., Part 2* **34**, L248 (1995); K. Fukushima, Y. Kanka, and T. Morishita, *J. Appl. Phys.* **74**, 6948 (1993).
- ²⁶See, for example, R. I. Dorn, *Am. Sci.* **79**, 542 (1991).
- ²⁷P. C. Hess, *Origins of Igneous Rocks* (Harvard University Press, Cambridge, 1989).
- ²⁸F. E. Lichte, *Anal. Chem.* **67**, 2479 (1995).
- ²⁹I. D. Kovalev, K. N. Malishev, and P. A. Shmonin, *J. Anal. Chem. USSR* **53**, 3842 (1998).